Boundary-Layer Meteorol (2016) 159:161–172
DOI 10.1007/s10546-015-0109-6

ARTICLE

Existence of Large Turbulent Eddies in the Early-Morning Boundary Layer Acting as an Effective Mountain to Force Mountain Waves

R. M. Worthington[1]

Received: 2 May 2015 / Accepted: 4 November 2015 / Published online: 17 November 2015

Abstract Numerical modelling suggests that the turbulent boundary layer can act as an effective mountain forcing mountain waves. In the daytime, convective rolls can cover the mountains, raising the mountain-wave launching height. In non-convective conditions, the nature of the effective mountain is unknown. Here, we investigate if the early-morning boundary layer, moving rapidly across mountains, also contains large eddies of size comparable with convective cells. Temperature profiles from thousands of high-resolution radiosondes show superadiabatic gradients of vertical scale a few hundred metres in the boundary layer, appearing as the boundary-layer wind speed increases. These are explained by the overturning of potential temperature surfaces in large eddies advected with the wind and/or longitudinal rolls. An early-morning satellite image shows longitudinal rolls over mountains up to 1 km height. It is suggested that early-morning fast-moving airflow over mountains, producing mountain waves, also creates a turbulent boundary layer underneath them containing large eddies of scale a few hundred metres, in addition to classic turbulence. These are part of the effective mountain, higher than the actual mountain, which explains the formation of mountain waves.

Keywords Mountain wave · Radiosonde · Turbulence

1 Introduction

Research on airflow over mountains has traditionally studied mountain waves in laminar, inviscid flow (neglecting the boundary layer), or turbulent flow (neglecting the mountain waves), the two research areas being kept separate (Wood 2000). Recently, numerical models have included a boundary layer (Jiang et al. 2006, 2008; Smith 2007; Smith and Skyllingstad 2009) but these are still essentially a modification of the Scorer (1949) theory, with the

✉ R. M. Worthington
rmw092001@yahoo.com

[1] Usk, South Wales, UK

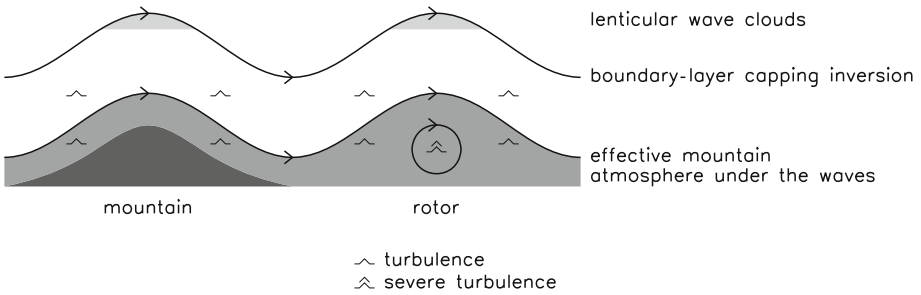

Fig. 1 Summary of a new paradigm to explain type 2 mountain waves (Peng and Thompson 2003; Worthington 2015). The lower part of the turbulent boundary layer acts as an effective mountain that can differ from the actual mountain. Often, only the smoother flow in the upper boundary layer, with a humidity maximum under the boundary-layer capping inversion, is revealed by lenticular mountain-wave clouds. The diagram shows two-dimensional flow, but the horizontal wind exhibits Ekman rotation with height, and the horizontal wavevector azimuth is centred on the wind direction across the effective mountain (Worthington 1999a, 2001). Adapted from Figs. 1, 2 of Förchtgott (1967) and Fig. 1 of Lester and Fingerhut (1974)

boundary layer acting as a 'sponge'. Large-eddy simulations such as Zhou and Chow (2014) are made over gentle terrain, rather than the other limiting case of high wind speeds over mountains.

In contrast, Peng and Thompson (2003) suggest that the turbulent boundary layer over mountains behaves as an effective mountain forcing mountain waves. This would explain why, for fairly isotropic mountains, the azimuthal distribution of the mountain-wave horizontal wavevector is centred on the horizontal wind vector at a height a few hundred metres above the mountain tops, as observed by Meso–Strato–Troposphere (MST) radar (Worthington 1999a, b) and satellites (Worthington 2001, 2006). The azimuthal distribution is centred on the wind vector at the 'mountain wave launching height' (Shutts 1997), where the flow becomes mostly wavelike instead of turbulent, or surface of the effective mountain.

Mountain waves can be classified as types 1 or 2 (Worthington 2014, 2015) depending on whether the effective mountain shape follows the shape of high ridge-like actual mountains, and the boundary layer can be neglected (type 1), or the effective mountain differs significantly from the actual mountain (type 2). Figure 1 summarizes the new paradigm for type 2 mountain waves. The lower part of the turbulent boundary layer acts as an effective mountain for the more wavelike flow above it. Only the smoother flow in the upper boundary layer is revealed by classic lenticular wave clouds. The rotor is included as an extreme case, for comparison with Fig. 1 of Lester and Fingerhut (1974).

Here, we investigate experimentally the nature of the lower turbulent layer in Fig. 1. Existence of mountain-wave rotors, effectively large turbulent eddies, is now accepted. Also, Worthington (2002) shows that the effective mountain can consist of convective rolls, another type of organized large eddy, above the mountains in daytime. These are known to create convection waves above flat ground (Young et al. 2002) and the similar waves above mountains appear indistinguishable from mountain waves, rather than being a distinct type of mountain convection wave (Bradbury 1990). Kalthoff et al. (1998) and Kossmann et al. (1998) report that the boundary-layer height follows the mountain height at some times of day. However, it is unknown whether the nighttime/early-morning boundary layer, fast-moving over mountains, contains classic turbulence or if large eddies are part of coherent structures such as longitudinal rolls.

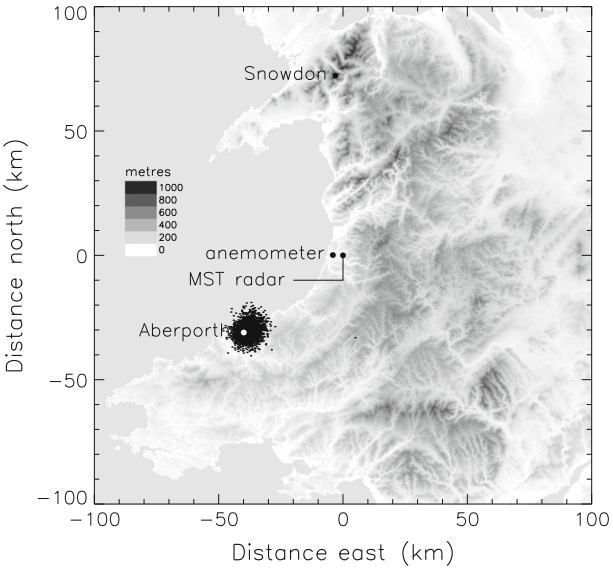

Fig. 2 Land height map centred on the Aberystwyth MST radar in Wales, UK, as in Worthington (2014), showing locations of a surface anemometer, and radiosonde launch site at Aberporth. *Dots* show horizontal locations at 2 km height of over 2500 radiosondes launched at 0500–0700 UTC, years 1991–2000

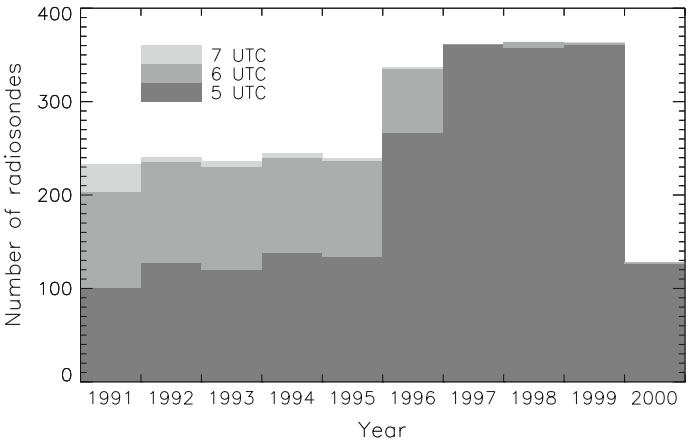

Fig. 3 Availability of early-morning radiosondes from Aberporth

1.1 Data

Locations of data sources, and land height, are shown in Fig. 2. Turbulent overturning in the boundary layer is shown by superadiabatic vertical temperature gradients (Clayson and Kantha 2008), using over 2500 radiosondes launched in the early morning at Aberporth (52.13°N, 4.57°W). Time resolution is 2 sec, with an ascent rate ≈5 m s^{-1} giving height resolution of ≈10 m; the surface wind speed is measured as 1-min averages by an anemometer on a 10-m tower at Frongoch Farm (52.42°N, 4.06°W). The data are too low in resolution

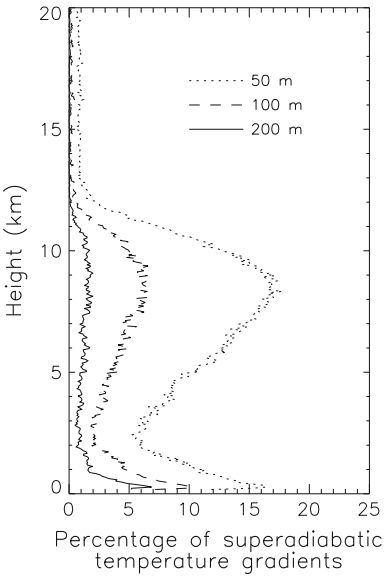

Fig. 4 Percentage probability of superadiabatic temperature gradients as a function of height using radiosondes at 0500–0700 UTC, years 1991–2000. Different height intervals of 50, 100 and 200 m are used for fitting the temperature gradient, to investigate the effect of random error causing spurious superadiabatic temperature gradients. The peak near 8 km height may be partly caused by random measurement error on the near-adiabatic temperature gradient in the upper troposphere. This almost disappears for the largest fitting interval of 200 m, and the remaining peak below 1-km height is caused by genuine turbulent overturning (Clayson and Kantha 2008)

to study small-scale turbulence, but are ideal for structures of scale a few hundred metres, similar to convective cells or longitudinal rolls.

Figure 3 gives the distribution of radiosonde launch times, at 0500–0700 UTC when the boundary layer is expected to be non-convective. Data at 2300 UTC are only available for 1996–2000 but give similar results. Mountain-wave vertical wind (w) is measured by the 46.5 MHz Aberystwyth MST radar using a vertical beam, averaged for 1 h to show the slowly-varying mountain-wave component. Four case studies show the dependence of mountain waves and their clouds on the surface wind and/or humidity profile. Type 1 modelling case studies of mountain waves above the region are shown by Shutts (1992), Vosper and Worthington (2002).

2 Results

2.1 Radiosondes

Since MST radar data commence at 1.7-km height, the effect of a turbulent boundary layer causing type 2 mountain waves has only been inferred. Radiosonde ascent rates have long been used to measure mountain-wave w oscillations (Laird 1952; Corby 1957; Shutts and Broad 1993; Shutts et al. 1994). However Clayson and Kantha (2008) show how standard high-resolution radiosondes can measure superadiabatic temperature gradients caused by convection, or overturning potential temperature surfaces in turbulent eddies. Wilson et al. (2011) report that potential temperature overturns down to 4-m scale can be measured.

Figure 4 shows the probability of superadiabatic temperature gradients less than –9.8 K km^{-1}, using fitting scales 50, 100 and 200 m. For 50- and 100-m fitting scales, there is an increased probability around 8-km height, and in the boundary layer. The increase around 8-km height may not be seen in browsing plots of MST radar vertical-beam spectral width corrected for beam broadening (Hocking 1985), and may be due to instrumental random error

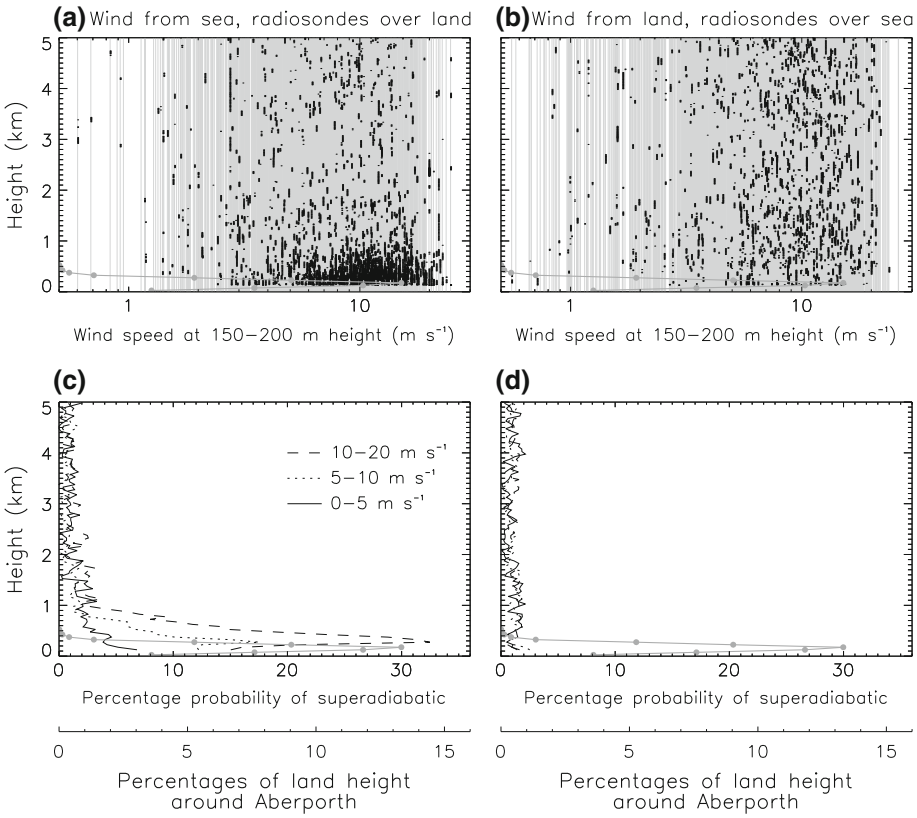

Fig. 5 Dependence of superadiabatic temperature gradients, fitted over 200-m height intervals, on wind speed measured by the same radiosondes at 150–200 m height. In **a**, **b** *vertical grey lines* show individual radiosondes, *black dots* show centre heights of superadiabatic temperature gradients. The coastline is approximately east-west, and the radiosondes are launched from a hill next to the sea, so **a**, **c** are for winds from the westerly–northerly–easterly 180° sector where the radiosondes mostly drift over land, and **b**, **d** are for easterly–southerly–westerly winds where the radiosondes mostly drift over sea. The land height histogram shown by *grey dots* is for a 50 × 50 km area centred on Aberporth

on the background temperature gradient, which is near adiabatic in the upper troposphere. Using a 200-m fitting scale, the increase at 8-km height almost disappears, but the increase within the boundary layer remains, implying results using 200 m may be physically realistic. Results are similar using a negative vertical gradient of potential temperature.

If superadiabatic gradients are the result of mechanically-forced large eddies, their probability should increase with low-level wind speed. Figure 5 shows superadiabatic gradients as a function of wind speed at 150–200 m height measured by the same radiosondes. The coastline is nearly east-west at the radiosonde launch site, which is a hill of maximum height 135 m, next to the sea. Repeating Fig. 5 for 45° azimuth sectors shows a difference for radiosondes above land and sea. Radiosonde data are therefore divided according to whether the low-level wind is from the sea (westerly–northerly–easterly 180° sector) and radiosondes drift over land, Fig. 5a,c, or from the land (westerly–southerly–easterly 180° sector) and radiosondes drift over sea, Fig. 5b,d.

For radiosondes over land, Fig. 5a,c, there is a dependence of superadiabatic gradients on wind speed (shown using a logarithmic scale to make the dependence clearer at low wind speeds). Below ≈3 m s^{-1}, the probability of superadiabatic gradients is low and shows little height dependence. Above ≈3 m s^{-1} there is a marked increase of occurrence in the boundary layer, reaching heights up to ≈1 km. However, for radiosondes over sea, Fig. 5b,d, there is no increased occurrence in the boundary layer.

This strong dependence on wind direction can be explained as hills inland from the launch site are smooth and only 100–150 m high, and southerly early-morning air flow has decoupled from the surface, with flow separation in valleys, so large eddies decay. In contrast, northerly sea-level airflow impacts upon steep sea-facing slopes and cliffs, which rise 100 m at a 45° slope (Ordnance Survey 2012), causing large eddies immediately downwind for airflow from sea to land. These large eddies could be spherical (Hooper et al. 1996) or part of longitudinal rolls (Etling and Brown 1993; Drobinski et al. 1998).

Figure 5c shows the probability of superadiabatic gradients as a function of height, for ranges of low-level wind speed. The probability of superadiabatic gradients increases with wind speed. For radiosondes at 1100 UTC and 1700 UTC, where the boundary layer is more convective, plots resemble Fig. 5a for both wind directions (not shown). Scorer (1954) shows a related effect at 1900 UTC where flow from land to sea produces large eddies rising as cumulus from a steep west-facing slope, heated by the sun and heath fires during the afternoon, the cumulus forming pileus wave clouds (Fig. 6). Figure 5a,c are for low-level flow in the opposite direction, striking steeper sea-facing slopes, apparently also creating large eddies in the early morning. Glider pilots report (Fig. 5 of Bishop 1966) that whereas stable airflow accelerates over a ridge, weakly stable airflow can break into thermals reaching over three times the height of the ridge.

2.2 AVHRR Satellite Images

Bradbury (1990) and Worthington (2002, 2005, 2006) show interacting convective rolls and type 2 mountain waves. The convective rolls are aligned with the mid-boundary-layer flow (Atkinson and Zhang 1996), and the mountain-wave phase lines are at right angles to them. This could appear counter-intuitive if the rolls are not corrugated in the direction of airflow. However, the mountain waves and rolls commonly interact (similar to convection waves tuning their own source) producing a pattern of bulges in the convective rolls, lined up across-wind, and in phase with the mountain-wave crests, acting as effective mountains (Worthington 2002, 2005, 2006).

Satellite images often show only one or the other cloud type; the relative height of maximum boundary-layer humidity and the mountain wave launching height determines which type of airflow is made visible by cloud. Humidity is often a maximum in the upper boundary layer under the capping inversion—above the mountain wave launching height, where the flow is wavelike causing wave clouds. In the afternoon, with a well-developed convective boundary layer, the mountain wave launching height is high (Worthington 2014) and the humidity maximum in the upper boundary layer sometimes reveals the tops of convective rolls, with invisible mountain waves above them only shown by MST radar (Worthington 2002, 2006).

Figure 7a,b shows two satellite images with longitudinal rolls and classic mountain-wave clouds respectively, both in the early morning. In Fig. 7a the roll clouds are above the Snowdonia mountains which reach over 1 km height (Fig. 2). There are also traces of mountain-wave modulation of the roll clouds. In Fig. 7b the horizontal wavelength near the anemometer is

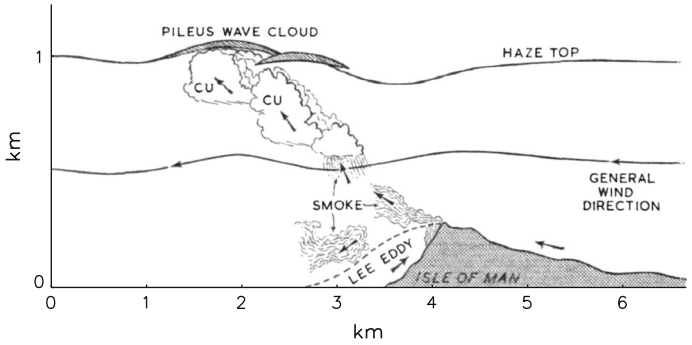

Fig. 6 Reprint from Scorer (1954) showing large eddies revealed by cumulus and smoke from heath fires, breaking away as the air flows up a mountain slope on the Isle of Man, at 1900 UTC, 25 April 1954. The rising cumulus forces waves and wave clouds. Vertical temperature gradient is superadiabatic over a height range more than 200 m. In Fig. 5a, c, the flow is instead from *left* to *right*, and in the early morning, up the steep sea-facing slope at Aberporth

9 km, which is typical of mountain waves. Wave clouds above the sea to the west are downwind of Ireland. The surface wind speed is 3–5 m s^{-1} and noisy in both Fig. 7c, d.

Upwind radiosonde profiles in Fig. 8a, within 1–2 h of the satellite images, both show vertical temperature gradients are stable in the lowest few km (about –6 K km^{-1}). Since the radiosondes only drift a few km horizontally in the boundary layer (Fig. 2) they may be more representative of the marine rather than mountain boundary layer. Horizontal wind profiles in Fig. 8b both show Ekman rotation and increasing wind speed with height, although with slightly higher wind speed for Fig. 7b. Given the similar time of day, cloud cover, boundary-layer stability and surface-wind noise, suggesting a similar boundary layer on the two days, it is surprising that Fig. 7a,b show very different clouds. However, Fig. 8c suggests an explanation.

The humidity for 25 April 1998 in Fig. 8c is a maximum in the lower boundary layer, whereas for 4 August 1998 it increases with height to a maximum at 280 m. Maximum humidity in the lower boundary layer is expected for calm foggy conditions, and is unusual for surface wind speed high enough to produce longitudinal rolls and/or mountain waves. This unusual humidity distribution reveals the turbulent atmosphere under the mountain waves, below the mountain wave launching height, in Fig. 7a. The more typical humidity distribution on 4 August 1998 reveals classic mountain-wave clouds, which could have a boundary layer as in Fig. 7a underneath them, not shown by cloud. Smooth lenticular wave clouds suggest laminar not turbulent flow, but this is an accident of the humidity distribution, only revealing the smooth wave flow above a turbulent lower boundary layer causing type 2 mountain waves (Fig. 1).

2.3 Anemometer

Wind gusts on time scales of seconds are explained by mechanical turbulence and daytime convection. Figure 5 implies large eddies of scale a few hundred metres, which if advected at a few m s^{-1} would be resolved by 1-min-average anemometer data. Figure 9 shows examples of calm and gusty surface wind, and w measured by MST radar. The gustiness, hereafter called 'noise', is estimated as the mean magnitude of the signal remaining after a 30-min running mean is subtracted. w is nearly zero in Fig. 9a, whereas Fig. 9b shows large slowly-

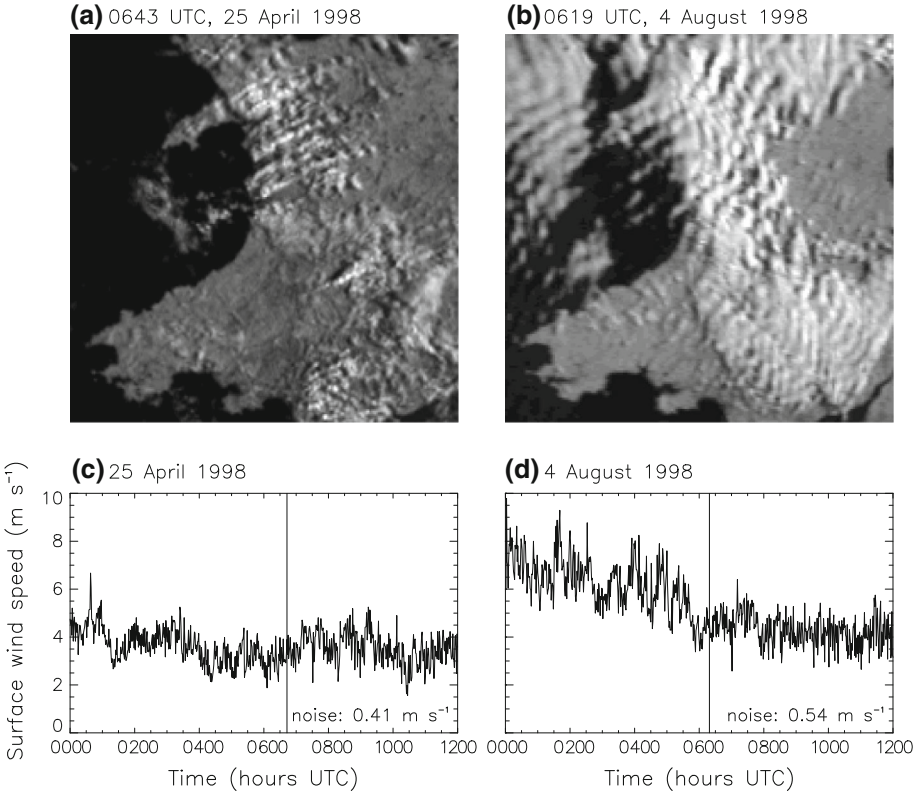

Fig. 7 **a**, **b** Visible-light AVHRR satellite images for the area in Fig. 2, showing **a** longitudinal roll clouds with traces of mountain-wave cloud, and **b** classic mountain-wave clouds. Surface wind is south-westerly in **a** and north-westerly in **b**. Sunrise is **a** 0458 UTC, **b** 0440 UTC. **c**, **d** show corresponding surface-wind time series measured by the anemometer in Fig. 2, which have similar wind speeds and noise at the times of the satellite images, marked by vertical lines. **a**, **b** are supplied by the Satellite Receiving Station, Dundee University, Scotland

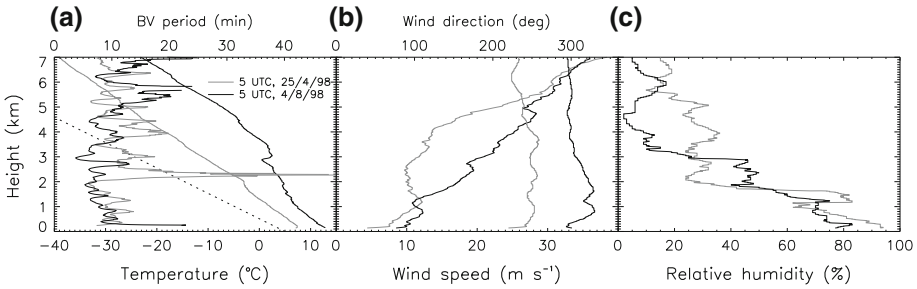

Fig. 8 Radiosonde profiles from Aberporth near the times of Fig. 7a, b. In **a** the *left* two lines are BV period and *right* two lines are temperature. In **b** the *left* two lines are wind speed and *right* two lines are wind direction. The *dashed line* in **a** shows the dry adiabatic temperature gradient. In the lowest few hundred metres, BV period and increase of horizontal wind speed with height are mostly similar for the two radiosondes

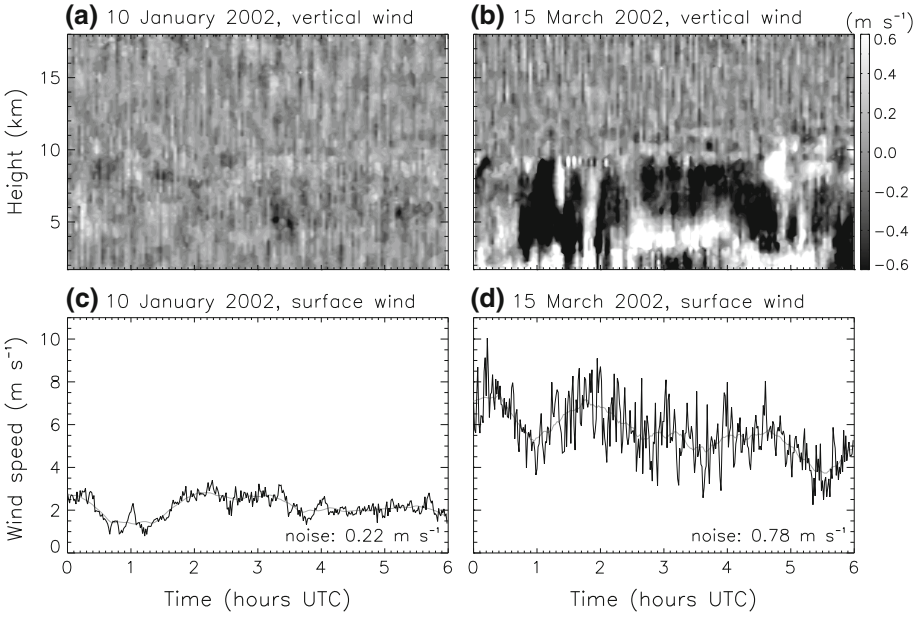

Fig. 9 **a**, **b** Height-time plots of w from MST radar, **c**, **d** surface wind time series in 1-min averages from anemometer (*black lines*), and smoothed by a 30-min running mean (*grey lines*). Noise is the mean magnitude of the signal remaining after the running mean is subtracted. Both case studies are for south-easterly flow over mountains. **a**, **c** show zero w and low surface winds with low noise, **b**, **d** show disturbed w from mountain waves up to 10-km height, for stronger surface winds with increased noise

changing w values characteristic of mountain waves, up to a critical layer at 10-km height (e.g. Fig. 5a of Worthington 2002). The superadiabatic gradients reach over 30 % probability in Fig. 5c, but the surface wind noise is continuous, suggesting a lower boundary layer filled with large eddies. The dependence of noise and mountain-wave w on surface wind speed and azimuth are compared below.

Figure 10a shows land height converted to azimuth and radial distance from the anemometer, to show the contrast of mountains and sea upwind. Surface-wind noise for 0000–0600 UTC in Fig. 10b increases with wind speed for all azimuths, with the largest increase for azimuth 000°–150° where there are mountains the shortest distance upwind, consistent with mechanical forcing of large eddies. There is a secondary peak near azimuth 300°; the anemometer is about 2 km inland, with hills of 100–150 m between its location and the sea. Sea-facing slopes rise 100 m at 45° slope with some cliffs, which could create turbulent eddies in westerly winds, advected across the anemometer.

Mountain-wave w measured at 2–5 km height by MST radar is shown in Fig. 10c. This uses all times of day, which is almost identical to 0000–0600 UTC but with less random error and data gaps. Figure 10c shows a similar pattern to Fig. 10b with the secondary peak near azimuth 300° suggesting that steep sea-facing slopes and cliffs are sufficient to create large eddies adding to the effective land height, to launch weak mountain waves from hills of only 100–150 m. Similarity of Fig. 10b,c only proves correlation rather than cause and effect between them, but is consistent with the turbulent boundary layer under mountain waves acting as an effective mountain to explain Worthington (1999a, 2001).

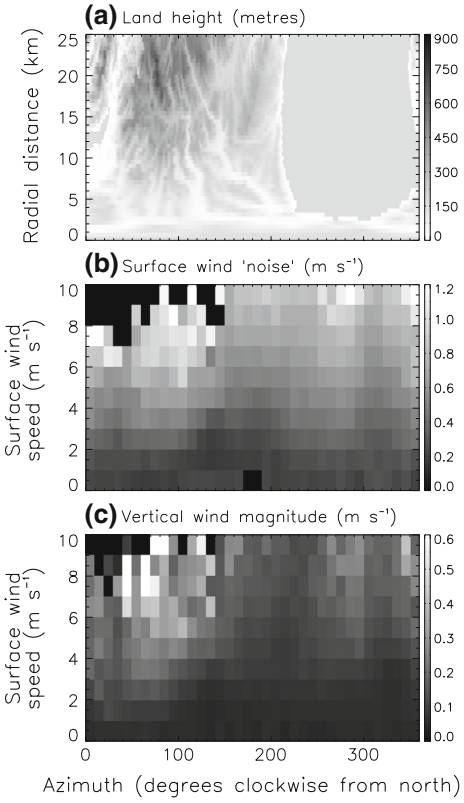

Fig. 10 **a** Land-height map centred on the anemometer, as a function of azimuth and radial distance, showing the contrast between directions with a low hill and sea upwind, and mountains upwind. **b** Dependence of surface-wind noise on hourly-averaged surface wind speed and azimuth measured by the anemometer. **c** Dependence of mean magnitude of w at 2–5 km height measured by MST radar, on surface-wind speed and azimuth as in **b**. *Black pixels* indicate data gaps

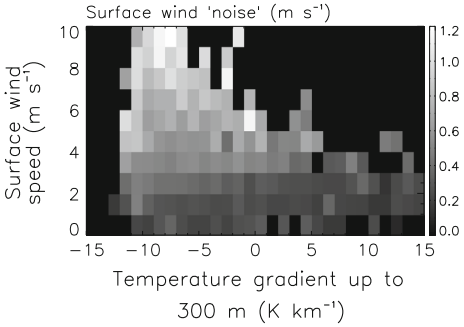

Fig. 11 Dependence of surface-wind noise on surface wind speed, and vertical temperature gradient from the minimum height ≈130 m up to 300 m measured by radiosondes. The increase of surface-wind noise with surface wind speed persists for a range of temperature gradients <zero, but for more stable temperature gradients >zero there are only low wind speeds with low noise

In Fig. 9 of Worthington (2015), both mountain-wave azimuth and Ekman rotation are only weakly dependent on boundary-layer temperature gradient in the range –10 to –3 K km^{-1}, which is explained by the occurrence of a turbulent boundary layer both acting as an effective mountain, and causing eddy viscosity with Ekman rotation. If consistent, surface-wind noise as in Fig. 10b is also expected over this range of temperature gradients in mountain-wave events.

Figure 11 shows the dependence of surface-wind noise on the vertical temperature gradient from a least-squares fit up to 300 m height. The highest surface wind speeds produce a near-adiabatic temperature gradient, but the increase of noise with wind speed still occurs up to

gradients of zero or higher. For the most stable temperature gradients, there are only low wind speeds and low noise. Surface-wind noise in Fig. 11 is therefore consistent with the turbulent boundary layer and explaining Fig. 9 of Worthington (2015).

Worthington (2014) reported a lack of diurnal variation in the mountain-wave amplitude, despite the diurnal changes of boundary layer between stable and convective. This might be explained since the nighttime and daytime mountain boundary layers, for wind speed high enough to cause mountain waves, are both filled with large eddies causing type 2 mountain waves. Repeating Fig. 10 for 1100–1700 UTC gives a similar pattern, as if the fast-moving mountain boundary layer contains large eddies at all times of day.

3 Conclusions

Radiosonde and surface anemometer data both indicate that the early-morning mountain boundary layer is filled with large eddies of scale up to a few hundred metres, for wind speeds high enough to force mountain waves. These are part of the effective mountain (Peng and Thompson 2003), which raises the mountain wave launching height above the surface (Fig. 1).

A satellite image soon after sunrise shows how these large eddies can take the form of longitudinal rolls, revealed by maximum humidity near the ground. Usually, humidity is maximum in the upper boundary layer, revealing wave clouds instead.

The similar dependence of surface-wind noise and mountain-wave w on the surface-wind vector suggests that conditions are similar to produce large eddies and mountain waves, and they often occur together, with a turbulent boundary layer containing large eddies below the mountain-wave flow.

Acknowledgments Radiosonde data are from the Met Office and British Atmospheric Data Centre. Natural Environment Research Council MST radar and surface-wind data are from BADC. AVHRR images are from the Satellite Receiving Station, Dundee University, Scotland. Thanks to Z K Olewicz, K Slater, Team TBE and Kubuntu, and Lakshmi Kantha for a sceptical review recommending publication.

References

Atkinson BW, Zhang JW (1996) Mesoscale shallow convection in the atmosphere. Rev Geophys 34:403–431
Bishop BB (1966) Mountain wave flow. Sailplane Gliding 17:3–8
Bradbury TAM (1990) Links between convection and waves. Meteorol Mag 119:112–120
Clayson CA, Kantha L (2008) On turbulence and mixing in the free atmosphere inferred from high-resolution soundings. J Atmos Ocean Technol 25:833–852
Corby GA (1957) A preliminary study of atmospheric waves using radiosonde data. Q J R Meteorol Soc 83:49–60
Drobinski P, Brown RA, Flamant PH, Pelon J (1998) Evidence of organised large eddies by ground-based doppler lidar, sonic anemometer and sodar. Boundary-Layer Meteorol 88:343–361
Etling D, Brown RA (1993) Roll vortices in the planetary boundary layer: a review. Boundary-Layer Meteorol 65:215–248
Förchtgott J (1967) Evidence for mountain-sized lee eddies. Weather 24:255–260
Hocking WK (1985) Measurement of turbulent energy dissipation rates in the middle atmosphere by radar techniques: a review. Radio Sci 20:1403–1422
Hooper WP, James JE, Lind RJ (1996) Lidar observations of turbulent vortex shedding by an isolated topographic feature. Boundary-Layer Meteorol 80:95–108
Jiang Q, Doyle JD, Smith RB (2006) Interaction between trapped waves and boundary layers. J Atmos Sci 63:617–633

Jiang Q, Smith RB, Doyle JD (2008) Impact of the atmospheric boundary layer on mountain waves. J Atmos Sci 65:592–608
Kalthoff N, Binder HJ, Kossmann M, Vögtlin R, Corsmeier U, Fiedler F, Schlager H (1998) Temporal evolution and spatial variation of the boundary layer over complex terrain. Atmos Environ 32:1179–1194
Kossmann M, Vögtlin R, Corsmeier U, Vogel B, Fiedler F, Binder HJ, Kalthoff N, Beyrich F (1998) Aspects of the convective boundary layer structure over complex terrain. Atmos Environ 32:1323–1348
Laird AR (1952) Standing wave at Aberporth. Meteorol Mag 81:337–339
Lester PF, Fingerhut WA (1974) Lower turbulent zones associated with mountain lee waves. J Appl Meteorol 13:54–61
Ordnance Survey (2012) Cardigan and New Quay Aberteifi a Cheinewydd Explorer Map No.198. Ordnance Survey, Southampton
Peng MS, Thompson WT (2003) Some aspects of the effect of surface friction on flows over mountains. Q J R Meteorol Soc 129:2527–2557
Scorer RS (1949) Theory of waves in the lee of mountains. Q J R Meteorol Soc 75:41–56
Scorer RS (1954) Isle of Man lee-wave. An unusual cloud formation seen during the I.C. meteorological expedition. Flight Aircr Eng 65:693–694
Shutts G (1992) Observations and numerical model simulation of a partially trapped lee wave over the Welsh mountains. Mon Weather Rev 120:2056–2066
Shutts G (1997) Operational lee wave forecasting. Meteorol Appl 4:23–35
Shutts G, Broad A (1993) A case study of lee waves over the Lake District in northern England. Q J R Meteorol Soc 119:377–408
Shutts GJ, Healey P, Mobbs SD (1994) A multiple sounding technique for the study of gravity waves. Q J R Meteorol Soc 120:59–77
Smith RB (2007) Interacting mountain waves and boundary layers. J Atmos Sci 64:594–607
Smith CM, Skyllingstad ED (2009) Influence of upstream boundary layer influence on mountain wave breaking and lee wave rotors using a large-eddy simulation. J Atmos Sci 66:3147–3164
Vosper SB, Worthington RM (2002) VHF radar measurements and model simulations of mountain waves over Wales. Q J R Meteorol Soc 128:185–204
Wilson R, Dalaudier F, Luce H (2011) Can one detect small-scale turbulence from standard meteorological radiosondes? Atmos Meas Technol 4:795–804
Wood N (2000) Wind flow over complex terrain: a historical perspective and the prospect for large-eddy modelling. Boundary-Layer Meteorol 96:11–32
Worthington RM (1999a) Alignment of mountain wave patterns above Wales: a VHF radar study during 1990–1998. J Geophys Res 104:9199–9212
Worthington RM (1999b) Calculating the azimuth of mountain waves, using the effect of tilted fine-scale stable layers on VHF radar echoes. Ann Geophys 17:257–272
Worthington RM (2001) Alignment of mountain lee waves viewed using NOAA AVHRR imagery, MST radar, and SAR. Int J Remote Sens 22:1361–1374
Worthington RM (2002) Mountain waves launched by convective activity within the boundary layer above mountains. Boundary-Layer Meteorol 103:469–491
Worthington RM (2005) Convective mountain waves above Cross Fell, northern England. Weather 60:43–44
Worthington RM (2006) Diurnal variation of mountain waves. Ann Geophys 24:2891–2900
Worthington RM (2014) Boundary-layer effects on mountain waves: a new look at some historical studies. Meteorol Atmos Phys 126:1–12
Worthington RM (2015) Type 1 and 2 mountain waves observed by MST radar and AVHRR. Meteorol Atmos Phys 127:325–331
Young GS, Kristovich DAR, Hjelmfelt MR, Foster RC (2002) Rolls, streets, waves, and more. A review of quasi-two-dimensional structures in the atmospheric boundary layer. Bull Am Meteorol Soc 83:997–1001
Zhou B, Chow FK (2014) Nested large-eddy simulations of the intermittently turbulent stable atmospheric boundary layer over real terrain. J Atmos Sci 71:1021–1039